Integrated Aero-Structural Optimization of Bio-Inspired and Generative AI Airfoils with Internal Lattice Architectures

Saahil P. Doshi*
Oconee County High School, Watkinsville, Georgia, 30677

Cashton Isaac†
Oconee County High School, Watkinsville, Georgia, 30677

Ramana Pidaparti, Ph.D.‡
University of Georgia, Athens, Georgia, 30606

This study presents an integrated aero-structural evaluation of bio-inspired and generative-AI airfoils for small-scale aircraft operating at low Reynolds numbers, a regime central to micro air vehicles (MAVs), drones, and small unmanned aerial systems (sUAS). Although airfoil optimization is well explored at the two-dimensional level, comparatively few studies examine how optimized shapes behave as real, finite wings with low aspect ratios especially when fabricated through additive manufacturing. This work addresses that gap by experimentally and computationally assessing bio-inspired, AI-generated, and conventional airfoils.

Three additively manufactured rectangular wings from peregrine falcon-inspired airfoil (GOE 265), a generative-AI geometry airfoil, and a conventional cambered NACA 5415 airfoil were tested at a zero angle of attack in an open-circuit wind tunnel at UGA across at freestream velocities of 8-15 m/s, corresponding to Reynolds numbers of approximately 5.5×10^4 to 1.55×10^5. All wings shared a common planform with extremely low aspect ratios (AR $\approx$ 0.32-0.75), representative of MAV/sUAS configurations. Experimental results showed substantial divergence from NeuralFoil (a data-driven model) section predictions due to the dominance of induced drag, tip-vortex losses, and aeroelastic interactions. GOE 265 achieved L/D ratios of 3-4 despite predicted values exceeding 20, while the AI-generated airfoil produced L/D $\approx$ 1.25-1.33 and became dynamically unstable above 10 m/s. These instability thresholds were treated as meaningful results, demonstrating how structural compliance and unsteady aerodynamics can constrain usable flight envelopes in lightweight UAV wings.

To enhance structural performance without modifying external aerodynamics, a bio-inspired internal Voronoi lattice modeled after sea-urchin stereo was integrated into the validated airfoil geometry. Finite-element simulations combined with a MATLAB-based machine learning workflow evaluated randomized lattice configurations to identify high strength-to-weight arrangements. The optimized lattice improved load survivability and was consistent with a bio-inspired wingbeat scaling law, showing that structurally efficient internal architectures can be embedded without compromising aerodynamic form. Overall, the results highlight three key insights for MAVs, drones, and small UAVs: (i) very low aspect ratio wings are dominated by induced drag and stability limits; (ii) experimentally observed instability boundaries offer critical constraints to aeroelastic effects; and (iii) bio-inspired internal lattices provide an effective approach for improving structural robustness while maintaining external aerodynamic geometry. The integrated experimental-computational methodology presented here offers a practical pathway for advancing small-scale aircraft design through simultaneous aerodynamic shaping, structural optimization, and additive manufacturing.

*High School Student, Oconee County High School, AIAA High School Student Member 1921410
†High School Student, Oconee County High School, AIAA High School Student Member 1921589
‡Faculty Advisor, University of Georgia, Associate Fellow

Nomenclature

b	wing span (model), m
c	chord length, m
S	planform area ($S = bc$), m^2
V	freestream velocity, m/s
ρ	air density, kg/m^3
μ	dynamic viscosity, Pa·s
Re	Reynolds number ($Re = \rho V c/\mu$)
L	lift force, N
D	drag force, N
q	dynamic pressure ($q = \frac{1}{2}\rho V^2$), Pa
C_L	lift coefficient ($C_L = L/(qS)$)
C_D	drag coefficient ($C_D = D/(qS)$)
L/D	lift-to-drag ratio
AR	aspect ratio ($AR = b/c$ for rectangular wings)
e	Oswald efficiency factor

I. Introduction

Small unmanned aircraft and student scale flight vehicles typically operate at low Reynolds numbers, a regime in which laminar separation bubbles, heightened sensitivity to transition, and geometry dependent stall behavior play a dominant role in aerodynamic performance. Although airfoil selection is often treated as a primary design variable under these conditions, experimental studies have shown that for small physical models and low aspectratio wings, three dimensional effects frequently dominate two dimensional airfoil behavior. Induced drag, mounting compliance, surface roughness associated with fabrication, and aeroelastic deformation can all significantly influence measured forces and moments, often to a greater extent than predicted differences between candidate airfoil sections [1] [2]. As a result, performance trends inferred from 2D airfoil data may not translate directly to student wind tunnel experiments or flight scale demonstrators.

Bio-inspired airfoil design offers an alternative pathway by drawing on wing sections evolved in birds to operate robustly across specialized flight envelopes, including low speed perching, gust rejection, and high lift maneuvering, as well as high speed dives. These natural airfoils frequently exhibit features such as aft loaded camber, blunt leading edges, or smoothly varying thickness distributions that may promote benign stall, delayed separation, or reduced sensitivity to Reynolds number compared with conventional engineering sections. In parallel, generative AI and optimization assisted workflows now enable rapid synthesis of novel airfoil geometries through parameterized camber and thickness representations or surrogate model based exploration of large design spaces. While these approaches dramatically lower the barrier to generating candidate shapes, they do not eliminate the need for careful experimental validation, particularly when bio-inspired or AI-generated airfoils are implemented as short, low aspect ratio wings in educational wind tunnel facilities, where three dimensional and mounting effects are unavoidable [3].

Beyond external aerodynamic shaping, additively manufactured wings introduce an additional and often underexplored internal structural architecture design. For lightweight printed wings, internal load paths, material distribution, and shell thickness directly influence structural compliance, which in turn can modify effective camber, twist, and stability boundaries under aerodynamic loading. This coupling motivates an integrated aerostructural design and testing framework in which both the external bioinspired airfoil geometry and the internal structural layout are treated as coequal design variables. Such an approach is particularly well suited to student-scale experiments, where structural flexibility is not merely a secondary effect but an integral part of the observed aerodynamic response.

The goal of this paper is to investigate an integrated aero-structural evaluation of bio-inspired and generative-AI airfoils for small-scale aircraft operating at low Reynolds numbers through experiments and computations. The scope and objectives of this investigation are presented below.

A. Objectives and scope

The objective of this study is to experimentally compare low Reynolds number, low aspect ratio finitewing performance at a fixed angle of attack ($\alpha = 0°$) across GenAI, bio-inspired, and conventional airfoil designs. Also, the measured experimental results of force trends, lift-to-drag (L/D) ratios for stable points, and stability limits, are compared against two dimensional NeuralFoil predictions to assess the dominance of induced drag and stability limits (stable vs. unstable behavior) [4]. Specifically, this paper provides a controlled comparison of low-Reynolds-number, finite-wing performance at a fixed $\alpha = 0°$ for:

1) **GenAI**: a generative-AI-produced airfoil geometry, exported as a coordinate file and fabricated as a rectangular wing.
2) **GOE 265**: a peregrine-falcon-inspired airfoil implemented using published GOE 265 airfoil coordinates.
3) **NACA 5415**: a conventional cambered baseline (NACA 5415).
4) **S1223**: a hawk-inspired high-lift airfoil (S1223) included for *computational* benchmarking only.

II. Methods

A. Wind-Tunnel Facility and Instrumentation

Testing was performed in a GUNT HM 170 open-circuit wind tunnel at UGA with a transparent test section and a two-component force sensor for lift and drag. Freestream velocity was set nominally to 8 m/s, 10 m/s, 13 m/s, and 15 m/s where stable operation was possible. The model angle of attack was constrained to $\alpha = 0°$ by a rigid mounting fixture attached to the force balance. Because the test article is a finite wing at very low aspect ratio, the balance, fixture, and exposed mounting hardware can contribute parasitic drag and introduce compliance that affects both the steady force readings and the onset of dynamic instability; these effects are treated explicitly in the interpretation of results.

(a) HM 170 wind tunnel and test section overview. **(b) Velocity measurement and manometer panel.** **(c) Force readout example (lift and drag channels).**

Fig. 1 UGA Experimental facility and instrumentation used for all test cases.

B. Wing Geometry and Planform

All physical wings were rectangular finite wings with a fixed span of 3 in (0.076,2 m). Chord length varied by configuration. Planform area was taken as $S = bc$ and aspect ratio as $AR = b/c$ for a rectangular planform. Table 1 summarizes the planform geometry used for coefficient calculations. The S1223 geometry is included because it was part of the computational comparison set, even though it was not tested in the tunnel [5].

Table 1 Planform geometry used for coefficient calculations (span fixed at 3 in).

Airfoil	b (in)	c (in)	S (m^2)	$AR = b/c$
GenAI	3.0	6.039	0.0117	0.50
GOE 265	3.0	6.0	0.0116	0.50
NACA 5415	3.0	4.0	0.0077	0.75
S1223	3.0	9.3	0.0180	0.32

These aspect ratios are intentionally very low, ensuring that induced drag and 3D effects are significant and that the test conditions are representative of compact lifting surfaces such as small UAV control surfaces or bio-inspired flaps.

C. Airfoil Models and Visualization

Figure 2 shows representative geometry renders for the four airfoil concepts used in this study.

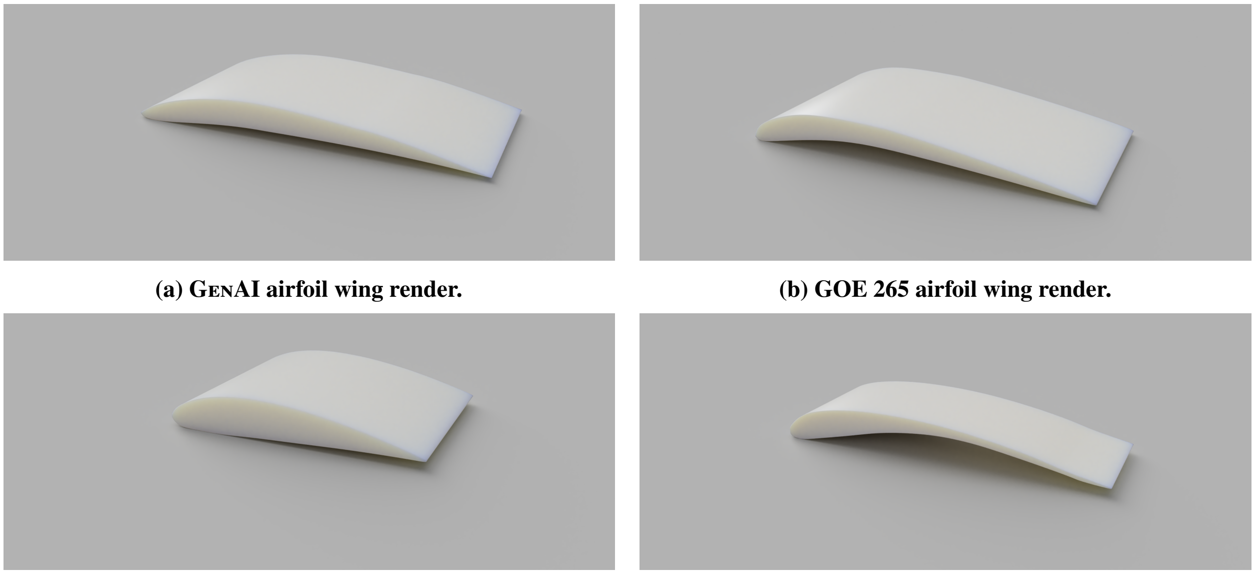

(a) GenAI airfoil wing render. **(b) GOE 265 airfoil wing render.**

(c) NACA 5415 baseline wing render. **(d) S1223 wing render.**

Fig. 2 Airfoil concepts included in this study (three tested experimentally; S1223 included computationally).

D. Experimental Procedure and Stability Classification

For each configuration and tunnel speed, the model was installed at $\alpha = 0°$ and the tunnel was allowed to reach steady operating conditions. Lift and drag readings were observed on the force balance display. Prior to recording, the procedure emphasized consistent setup (model installation and fixture alignment) so that comparisons across airfoils reflect geometry-driven behavior rather than large changes in setup conditions.

If the wing reached a visibly steady operating condition with stable sensor readings, the time-averaged lift and drag were recorded. If the wing exhibited strong dynamic instability (for example, violent oscillation, buffeting, or persistent shaking of the mount) that prevented a clear steady reading, the condition was labeled *Unstable* and excluded from coefficient calculation. This binary classification captures the practical operating envelope of each configuration in the given setup.

E. Data Reduction

For stable operating points, dimensional forces were converted to nondimensional coefficients using standard relations:

$$q = \frac{1}{2}\rho V^2, \tag{1}$$

$$C_L = \frac{L}{qS}, \tag{2}$$

$$C_D = \frac{D}{qS}, \tag{3}$$

$$Re = \frac{\rho V c}{\mu}. \tag{4}$$

Unless otherwise stated, calculations used $\rho = 1.225\,\mathrm{kg/m^3}$ and $\mu = 1.81 \times 10^{-5}\,\mathrm{Pa \cdot s}$. These values represent standard sea-level assumptions; the resulting coefficients should therefore be interpreted as approximate but consistent across configurations.

F. Measurement Uncertainty and Repeatability

Uncertainty is dominated by (i) force-balance reading variability in L and D and (ii) freestream velocity uncertainty through $q = \frac{1}{2}\rho V^2$. Because the dataset emphasizes stability-limited operation at fixed $\alpha = 0°$, multiple independent repeats were not collected for every condition; instead, points were recorded only when the readouts reached a steady range, and conditions that did not were classified as *Unstable*. For stable points, first-order coefficient bounds follow:

$$\delta C_L \approx C_L \sqrt{\left(\frac{\delta L}{L}\right)^2 + \left(\frac{\delta q}{q}\right)^2 + \left(\frac{\delta S}{S}\right)^2}, \tag{5}$$

$$\delta C_D \approx C_D \sqrt{\left(\frac{\delta D}{D}\right)^2 + \left(\frac{\delta q}{q}\right)^2 + \left(\frac{\delta S}{S}\right)^2}, \tag{6}$$

with $\delta q/q \approx \sqrt{(\delta\rho/\rho)^2 + (2\,\delta V/V)^2}$. Future work should document balance resolution and collect repeats to report explicit uncertainty bars on C_L, C_D, and L/D.

G. Computational Analysis through NeuralFoil Software

Two-dimensional section coefficients at $\alpha = 0°$ were estimated using NeuralFoil via AeroSandbox [6]. NeuralFoil is a data-driven surrogate intended to reproduce XFOIL-like trends over relevant parameter ranges [7]. The interface used here employs its default transition and roughness assumptions, which are broadly comparable to a clean airfoil analysis with a typical XFOIL N_{crit} value [8]. At low Reynolds number, section predictions can be sensitive to transition/roughness assumptions; consequently, NeuralFoil results are used to contextualize trends and set an upper bound rather than to exactly match finite-wing measurements.

Reynolds numbers were selected to match the experimental chord and speed conditions as closely as possible for GenAI, GOE 265, and NACA 5415. Additional Reynolds points were included for GOE 265 and S1223 to show trends over the low-Re range of interest. Because NeuralFoil provides section coefficients, the results do not include induced drag or other finite-wing corrections; they are interpreted as an upper bound on achievable performance for the implemented geometries.

III. Results

The results of wind-tunnel experiments as well as computational analysis obtained are presented below.

A. Wind-Tunnel Force Measurements

Table 2 reproduces the full wind-tunnel dataset (forces in Newtons). "Unstable" indicates that a steady reading was not obtainable due to dynamic instability in the model or mounting.

Table 2 Measured wind-tunnel lift and drag forces (stable points and unstable conditions).

	$V = 8$ m/s		$V = 10$ m/s		$V = 13$ m/s		$V = 15$ m/s	
Airfoil	L (N)	D (N)	L (N)	D (N)	L (N)	D (N)	L (N)	D (N)
GenAI	0.05	0.04	0.08	0.06	Unstable		Unstable	
GOE 265	0.19	0.06	0.27	0.08	0.42	0.12	0.54	0.16
NACA 5415	0.07	0.03	0.11	0.05	Unstable		Unstable	

B. Derived Coefficients and Reynolds Numbers

Table 3 reports Reynolds numbers and aerodynamic coefficients for stable operating points only. The NACA 5415 Reynolds number at 8 m/s is on the order of 5.5×10^4 rather than 5.5×10^5, consistent with its shorter chord.

C. Measured Trends vs. Velocity

Figures 3a–3c summarize the measured forces and aerodynamic efficiency versus freestream speed for all stable cases.

Table 3 Experimental Reynolds numbers and aerodynamic coefficients (stable points only).

Airfoil	V (m/s)	Re	C_L	C_D	L/D
GenAI	8	83,051	0.109	0.087	1.25
GenAI	10	103,814	0.112	0.084	1.33
GOE 265	8	82,490	0.418	0.132	3.17
GOE 265	10	103,113	0.380	0.112	3.38
GOE 265	13	134,087	0.349	0.100	3.50
GOE 265	15	154,669	0.337	0.100	3.38
NACA 5415	8	55,010	0.232	0.099	2.33
NACA 5415	10	68,762	0.232	0.105	2.20

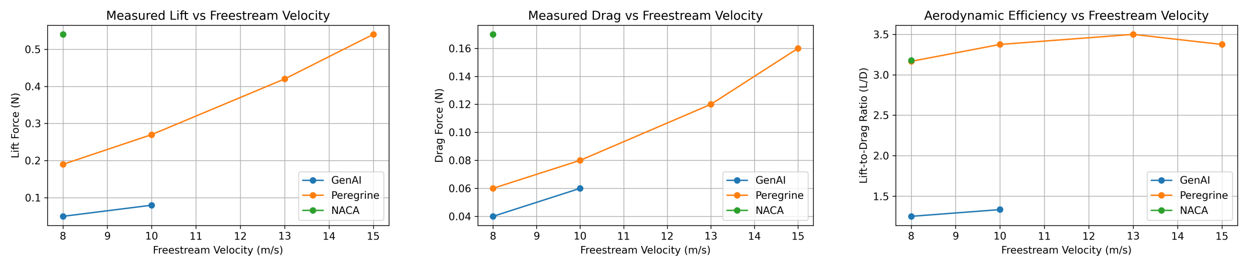

(a) Lift vs. velocity. **(b) Drag vs. velocity.** **(c) L/D vs. velocity.**

Fig. 3 Measured forces and aerodynamic efficiency versus freestream velocity (stable points only).

D. NeuralFoil (2D Section) Predictions at $\alpha = 0°$

Table 4 reports NeuralFoil predictions for the analysis matrix. These are *2D section* coefficients and do not include induced drag or other finite-wing corrections.

Table 4 NeuralFoil 2D section coefficient estimates at $\alpha = 0°$.

Airfoil	Re	N_{crit}	C_L	C_D	L/D
GenAI	83,100	9	0.090	0.063	1.42
GenAI	103,800	9	0.299	0.075	4.00
GOE 265	82,500	9	0.644	0.029	22.48
GOE 265	103,100	9	0.659	0.025	26.06
GOE 265	134,100	9	0.664	0.022	30.33
GOE 265	154,700	9	0.665	0.020	33.03
NACA 5415	55,000	9	0.232	0.045	5.20
S1223	100,000	9	1.239	0.023	54.19
S1223	150,000	9	1.231	0.020	62.19

IV. Bio-Inspired Internal Lattice Structural Analysis

The wind-tunnel experiments demonstrated that dynamic stability can become a practical limiter for lightweight, additively manufactured wings in very low-AR configurations, with GenAI and NACA 5415 exhibiting instability above 10 m/s in the present mounting setup. Motivated by this constraint, the following section explores internal architectures as a pathway to improve stiffness and load survivability *without* modifying external aerodynamic geometry, enabling more robust structures that can support more repeatable aerodynamic testing in future work.

Beyond the bio-inspired shaping, the performance of an airfoil can be further optimized through internal supports derived from biological structures. Traditional airfoils are typically comprised of spars and ribs, structures designed to resist bending and support stress/strain loads. In looking towards naturally occurring structures that undergo similar load types, a bio-inspired substitute can be explored and optimized as an alternative solution to support the airfoil.

Naturally occurring structures can be grouped into three subcategories: cellular, fibrous, and sandwich. Cellular structures are characterized by their repeated cellular geometry, optimizing a strength-to-weight ratio via empty cells. Fibrous structures are defined by their use of cylindrical fibers to create rigid structures via bundles or lamellae. Lastly, sandwich structures are known for their use of a tough, outer shell that protects a softer, lighter porous inside (Zhang et al., 2023). [9]

Among research biological candidates, including pomelo peel, glass sponge skeletons, vulture wings, and woodpecker beaks, the sea urchin exoskeleton demonstrated the most adaptable structure for the airfoil. Studies on the mechanical properties inside the exoskeleton of the sea urchin have shown that its internal structure, known as Voronoi, demonstrates great strength and rigidity for its porous, cellular structure (Efstathiadis, 2022).[10] By using Voronoi as a template for a bio-inspired structure for the airfoil, a lattice can be derived and used to support the outer skin shape.

A volumetric Voronoi model was generated in Rhinoceros 3D (Rhino) using Grasshopper's 3D Voronoi block. To identify common structural patterns, a cubic Region of Interest (ROI) tool was implemented in MATLAB to isolate cubic subregions from the larger Voronoi volume from Rhino. Repeated sampling revealed a characteristic geometry consisting of a dense, central core with radial struts extending toward the boundaries of the cube.

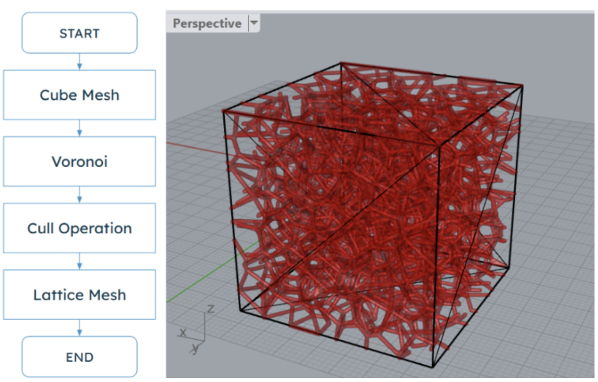

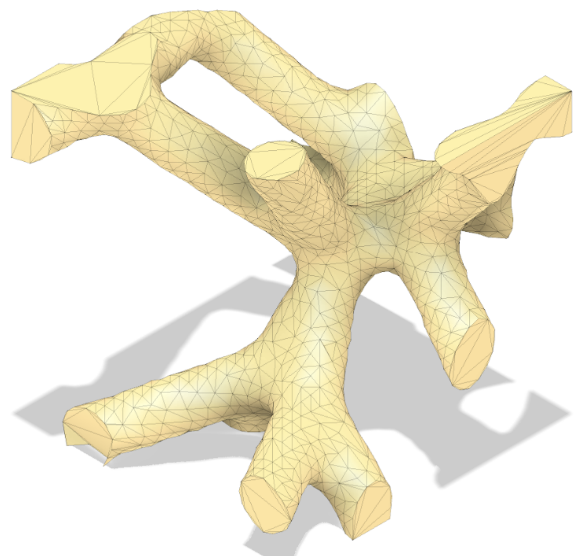

(a) Modeled Voronoi output. **(b) Example of a common pattern found using the ROI tool.**

Fig. 4 Workflow of Voronoi creation and modeled Voronoi output (Left) and example of a common pattern found using the ROI tool (Right).

With this common geometry as a base design inspiration, unit cubes could be developed following the structure of Voronoi. This is how the three unit cubes, Mk. 2, 3, and 4, were created. Each cube retains a central core but differs in strut configuration. Mk. 2 employs a dominant diagonal strut supplemented by smaller, secondary supports. Mk. 3 redistributes support toward face and edge connections with three struts stemming from its core. Mk. 4 implements symmetric corner-directed struts with four struts going to all four corners on each face. In designing these as unit cells, each cube can be iteratively stacked, placed, or interchanged with the others to create a grid network inside the airfoil.

With the unit cubes created, they were then arranged within the previously developed bio-inspired airfoil geometry using uniform cubic placement at a scale factor of 0.9 relative to the airfoil. Each cube can be placed in this format to create a continuous lattice network inside the airfoil.

To determine the best placement of each cube in this format, a convergence-based optimization process was implemented. Finite element analysis (FEA) simulations were conducted in Autodesk's Fusion via cantilever analysis with the root fully constrained and a 100 N point load applied at the wing tip. Maximum Von Mises stress and maximum 1st Principal stress were extracted for each configuration.

To achieve solution convergence, the simulation workflow was coupled with MATLAB's Statistics and Machine Learning Toolbox. A machine learning program in MATLAB suggested batches of 10 configurations of unit cubes to be analyzed in FEA. The results were fed back to the program, and it would suggest a new batch based on a normalized

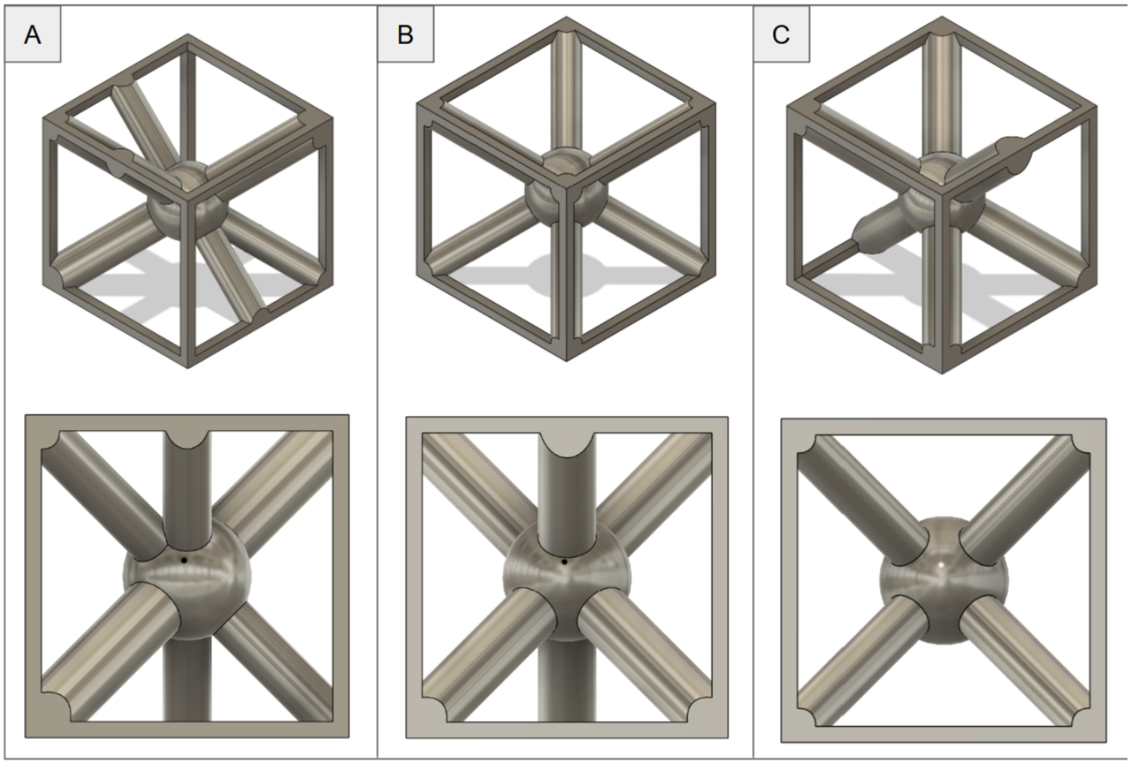

Fig. 5 Mk. 2 (A), Mk. 3 (B), and Mk. 4 (C).

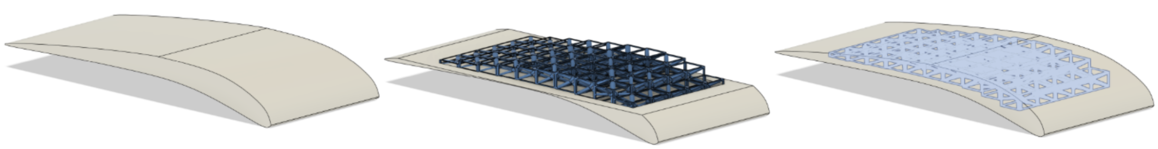

Fig. 6 Unit cubes placed in the airfoil to create a lattice network.

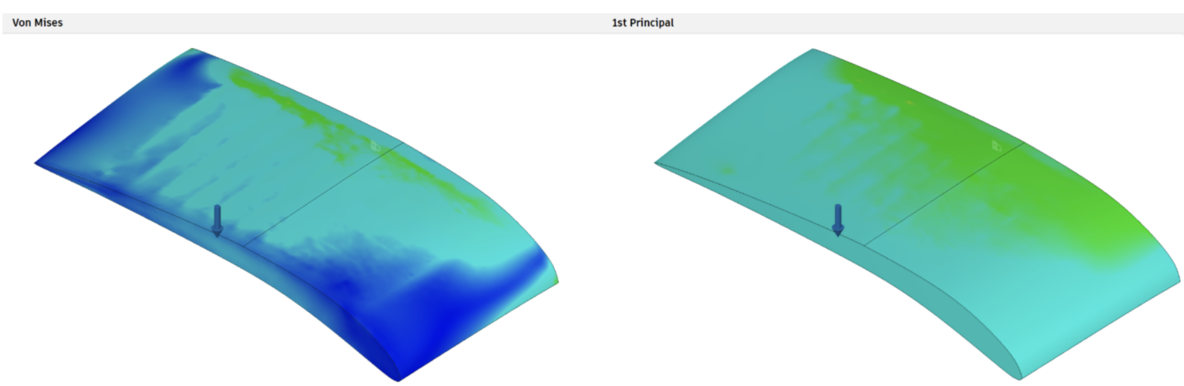

Fig. 7 Example of Von Mises and 1st Principal stress FEA Results on cantilever analysis.

multi-objective score constructed from the maximum stress results. This iterative process was repeated for 100 total simulations.

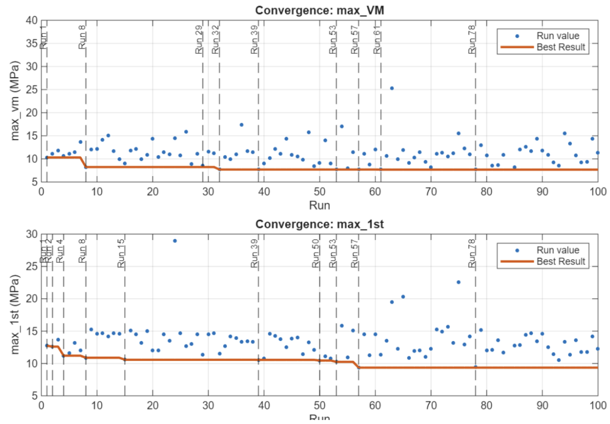

(a) **Convergence plots for maximum Von Mises and 1st Principal stresses.**

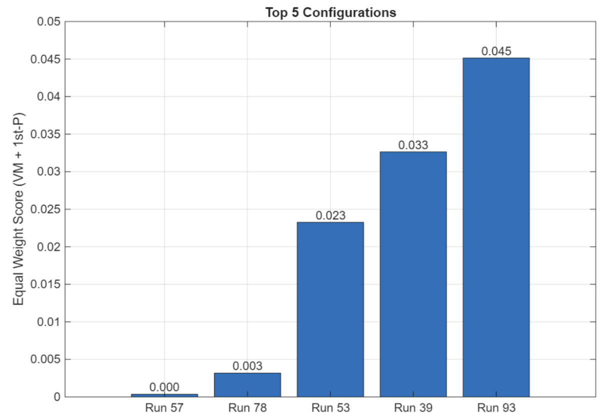

(b) **Top 5 configurations with normalized VM and 1st results.**

Fig. 8 Convergence plots for maximum Von Mises and 1st Principal stresses (left) and Top 5 configurations with normalized VM and 1st results (right).

Via this machine learning optimization process through convergence analysis, the most optimal result was found in Run 57 with its unique placement of unit cubes. This run reduced maximum Von Mises stress by 26% and maximum 1st Principal stress by 14% relative to the best-performing configuration in the initial batch of 10 simulations.

This iterative refinement process mirrors evolutionary selection principles, in which high-performing structural configurations are retained while inefficient geometries are discarded. Through this process, a structurally optimized, bio-inspired lattice was successfully integrated into the airfoil geometry.

Table 5 Summary of reported stress improvements for the optimized lattice configuration (Run 57).

Metric	Improvement (relative to best of initial batch)
Maximum Von Mises stress	26% reduction
Maximum 1st Principal stress	14% reduction

V. Discussion

A. Finite-Wing Effects and the GOE 265 Performance Gap

The large gap between the NeuralFoil predictions and the measured GOE 265 coefficients is expected because the experiment uses extremely low-aspect-ratio wings (Table 1). At such low AR, induced drag is large and the effective lift curve slope is reduced relative to a 2D section. A common induced drag estimate is

$$C_{D,i} = \frac{C_L^2}{\pi e AR}, \tag{7}$$

which increases rapidly as AR decreases. Using the measured C_L values for GOE 265 and $AR \approx 0.5$, Eq. (7) yields induced drag contributions on the order of 10^{-1} for an Oswald factor e of order unity, consistent with the measured $C_D \approx 0.10$ at higher speeds. This explains why the measured GOE 265 L/D remains near 3–4 while the 2D section L/D predicted by NeuralFoil is much larger.

B. Interpretation for the Generative AI Airfoil

For GenAI, the measured C_L values at $\alpha = 0°$ are relatively small, so induced drag is less dominant than for GOE 265. The measured C_D therefore reflects a combination of profile drag plus parasitic contributions (surface roughness, mounting interference, and low-AR vortex losses). The result is a persistently low measured L/D (1.25–1.33) even when the 2D model predicts improved performance at higher Reynolds number. The additional observation that

GenAI became unstable above 10 m/s indicates that practical structural and aeroelastic behavior limited the usable test envelope for this concept.

C. Aero-Structural Implications of Internal Lattice Architectures

The structural results from the bio-derived lattice demonstrate an alternative internal airfoil architecture that prioritizes strength-to-weight efficiency through its biological design inspiration. In implementing manufacturable unit cube designs as modular building blocks, the resulting framework emulates a porous sandwich morphology analogous to sea urchin stereom. Through iteratively unit cube placement, the machine learning-guided convergence analysis produced measurable reductions in two key stress metrics. This framework, therefore, presents an alternative to traditional spars and ribs by employing a biologically inspired methodology for stress distribution and minimization. While the wind-tunnel dataset in this study does not directly quantify stiffness or stability improvements, the demonstrated lattice workflow reinforces the biologically-inspired design methodology of the best-performing airfoil shape. As a result, the integrated shape and structure of the bio-inspired airfoil yielded strength and aerodynamic results favoring optimized performances, offering a scalable design approach for manufactured wings.

D. Stability as a Practical Design Discriminator

A key empirical outcome is that stability limits separated the designs: GOE 265 remained stable across 8 m/s to 15 m/s, whereas GenAI was unstable above 10 m/s and NACA 5415 was unstable above 10 m/s. For student-scale, 3D-printed wings in educational wind tunnels, stiffness, mounting compliance, and vortexes can determine whether meaningful force measurements are possible at all. In practical design work, an airfoil that is theoretically efficient but dynamically unstable in a given configuration can be inferior to a slightly less efficient but robustly stable design.

E. Implications for Low-Re Design Workflows

Taken together, the experimental, computational, and structural results suggest a practical workflow for low-Re airfoil studies using student-scale facilities:

1) Use NeuralFoil (or XFOIL where available) to screen 2D section performance at Reynolds numbers matched to the intended chord and operating speeds.
2) Convert 2D predictions into approximate finite-wing expectations using the known aspect ratio and induced drag estimates such as Eq. (7), setting realistic bounds on achievable L/D.
3) Design mounts and test articles to maximize stiffness and minimize unwanted degrees of freedom, then validate with wind-tunnel testing, focusing initially on stability and repeatability rather than a dense polar.
4) Where additive manufacturing is used, evaluate internal lattice architectures to improve stiffness and stress distribution without changing external aerodynamic geometry.

This approach reduces the risk of over-interpreting optimistic 2D L/D values when the physical test article is a very low-AR wing and emphasizes the importance of structural and mounting design alongside airfoil selection.

F. Limitations and Future Work

This study is intentionally narrow in operating condition (fixed $\alpha = 0°$) and includes stability-limited datasets for some wings. The coefficients rely on assumed air properties and a single set of runs without explicit uncertainty propagation. Future work should prioritize:

1) repeat trials and force sensor tare/zero verification at each speed to bound measurement uncertainty,
2) documentation of force balance resolution/least-count and the observed steady reading range for stable points,
3) redesign of the mounting hardware to increase stiffness and reduce vibration,
4) expanded angle-of-attack sweeps to obtain full lift and drag polars and stall behavior,
5) experiments with endplates or higher aspect ratio wings to reduce induced-drag dominance and better isolate profile performance,
6) direct experimental comparison of identical external airfoils with different internal lattice architectures to quantify stiffness-driven stability changes.

VI. Conclusions

A comparative evaluation of a generative-AI airfoil (GenAI), a peregrine-falcon-inspired airfoil (GOE 265), and a baseline cambered airfoil (NACA 5415) was conducted using a constrained $\alpha = 0°$ wind-tunnel campaign with supporting NeuralFoil computations. The GOE 265 wing produced the most consistent and stable measured performance across all tested speeds, with L/D between 3.17 and 3.50. The GenAI wing produced lower measured L/D (1.25–1.33) and became unstable above 10 m/s. For the NACA 5415 wing, stable measurements were obtained at 8 m/s and 10 m/s with lower measured L/D relative to GOE 265 under the same constrained $\alpha = 0°$ condition.

On the structural side, a bio-inspired Voronoi-derived internal lattice architecture was integrated into the airfoil geometry and optimized through FEA coupled with a MATLAB-based machine learning workflow. The optimized configuration (Run 57) reduced maximum Von Mises stress by 26% and maximum 1st Principal stress by 14% relative to the best-performing configuration in the initial batch.

Overall, the work emphasizes that (i) very low-aspect-ratio testing requires explicit finite-wing interpretation when comparing against 2D section predictions, and (ii) aeroelastic stability and internal structural design can be as important as nominal airfoil efficiency when validating small, additively manufactured wings for low-Reynolds-number applications.

Acknowledgments

The authors acknowledge the faculty and staff at UGA for their support of the wind-tunnel testing phase. This study also employed OpenAI's ChatGPT for the GenAI airfoil profile and for enhancing the clarity and phrasing of the text.

Data Availability Statement

All wind-tunnel force measurements used in this paper are reproduced in Table 2. The NeuralFoil analysis matrix used for Table 4 was generated from the Python workflow and exported to CSV.

References

[1] Han, J., Chen, G., Tian, F., and Hui, Z., "Review on bio-inspired flight systems and bionic aerodynamics," *Chinese Journal of Aeronautics*, 2019. URL `https://doi.org/10.1016/j.cja.2020.03.036`.

[2] Moitra, S., Kiran, J. V. S., Raghavendra, G. S. G., and Sudheer, A. P., "Design and Analysis of a Bio-inspired Flapping Wing Robot," *Proceedings of the 2017 3rd International Conference on Advances in Robotics*, Association for Computing Machinery, New York, NY, USA, 2017. https://doi.org/10.1145/3132446.3134892, URL https://doi.org/10.1145/3132446.3134892.

[3] Agrawal, A., and Agrawal, S., "Design of Bio-inspired Flexible Wings for Flapping-Wing Micro-sized Air Vehicle Applications," *Advanced Robotics*, Vol. 23, No. 11, 2009, pp. 1481–1495. https://doi.org/10.1163/156855309X443133.

[4] Sharpe, P. D., "NeuralFoil: Airfoil Aerodynamics via Machine Learning (Software Repository)," https://github.com/peterdsharpe/NeuralFoil, 2024.

[5] Selig, M. S., and collaborators, "UIUC Airfoil Coordinates Database," https://m-selig.ae.illinois.edu/ads/coord_database.html, 1994.

[6] Sharpe, P. D., "AeroSandbox (Python Package)," https://pypi.org/project/aerosandbox/, 2025.

[7] Drela, M., "XFOIL: An Analysis and Design System for Low Reynolds Number Airfoils," Tech. rep., Massachusetts Institute of Technology, 1989.

[8] Sharpe, P. D., "Aircraft Design Optimization and Aeroelastic Analysis with AeroSandbox," Ph.D. thesis, Massachusetts Institute of Technology, 2024.

[9] Zhang, Z., Mu, Z., Wang, Y., Song, W., Yu, H., Zhang, S., Li, Y., Niu, S., Han, Z., and Ren, L., "Lightweight Structural Biomaterials with Excellent Mechanical Performance: A Review," *Biomimetics*, Vol. 8, No. 2, 2023. https://doi.org/10.3390/biomimetics8020153, URL https://www.mdpi.com/2313-7673/8/2/153.

[10] Efstathiadis, A., Symeonidou, I., Tsongas, K., Tzimtzimis, E. K., and Tzetzis, D., "Parametric Design and Mechanical Characterization of 3D-Printed PLA Composite Biomimetic Voronoi Lattices Inspired by the Stereom of Sea Urchins," *Journal of Composites Science*, Vol. 7, No. 1, 2023. https://doi.org/10.3390/jcs7010003, URL https://www.mdpi.com/2504-477X/7/1/3.